Understanding the Dynamics of Fluorescence Emission During Zeolite Detemplation Using Time Resolved Photoluminescence Spectroscopy

Naomi Omori†, Alex G. Greenaway†※, Misbah Sarwar⁑, Paul Collier ⁑, Gianluca Valentini‡‖, Andrew M Beale †※*, Alessia Candeo**

†Department of Chemistry, University College London, 20 Gordon Street, London, WC1H 0AJ, UK

⁑Johnson Matthey Technology Centre, Blounts Court, Sonning Common, RG4 9NH, UK

*Central Laser Facility, Science and Technology Facilities Council, Research Complex at Harwell, Didcot, Oxfordshire, OX11 0FA, UK

‡Dipartimento di Fisica, Politecnico di Milano, Piazza Leonardo da Vinci 32, I-20133 Milano, Italy

‖Istituto di Fotonica e Nanotecnologie, Consiglio Nazionale delle Ricerche, Piazza Leonardo da Vinci, I-20133 Milano, Italy

※ Research Complex at Harwell, Rutherford Appleton Laboratory, Didcot, Oxfordshire, OX11 0FA, UK

ABSTRACT

Time-resolved photoluminescence spectroscopy (TRPS) shows potential as a sensitive, non-destructive, high throughput, label-free laser-based spectroscopy technique capable of analysing low concentrations of organic species adsorbed on and within zeolite pores. Here we report the results from a study that uses TRPS to characterise photoluminescence (PL) arising from synthesised chabazite framework zeolites at three different stages of the detemplation process (from an uncalcined, partially calcined, and calcined zeolite). Temporal resolution was used to demonstrate the steric confinement effects of OSDA within a zeolite framework and therefore to establish a signature region for determining the presence of the template. Gated spectra comparisons between an uncalcined and a partially calcined zeolite demonstrated the presence of template alongside the proliferation of template-derived combustion products. An analysis of lifetime values demonstrated the ability for TRPS to track depletion of OSDA and establish a characteristic PL spectrum for a clean zeolite. The sensitivity of the technique is high enough to reveal that there is still residual organic material remaining in a zeolite even after an extended thermal detemplation process.

1. INTRODUCTION

Zeolites are porous aluminosilicates that are fundamental in catalysing a series of high interest industrial reactions such as fluid catalytic cracking in oil refineries[1], which accounts for over 95 % of zeolite consumption in industrial catalysis, and the methanol-to-olefins reaction[2], which has recently been commercialised in China's rapidly growing chemical industry[3]. When studying catalytic zeolite systems, it is important to differentiate between the 'phases' of interest: the crystalline aluminosilicate framework; adsorbed organic species; and gas-phase catalytic reactant products. Framework structure and composition are characterised effectively using the well-established triumvirate of X-ray diffraction (XRD), electron microscopy, and nuclear magnetic resonance (NMR) techniques, whereas gas-phase reactant products coming off the zeolites may be analysed using mass spectrometry (MS) or gas chromatography (GC). However, organic species adsorbed within zeolite pores are comparatively difficult to measure using these aforementioned techniques due to their diminutive molecular weight that is challenging to resolve in SEM or TEM, oftentimes low concentration that limits usage of ^{13}C NMR[4], and location within the framework. Rather than relying on any single analytical technique[5], the complexities of adsorbed organic species necessitate a broad, multimodal approach utilising numerous characterisation methods. Thermal methods, such as thermogravimetric analysis (TGA) and temperature programmed oxidation (TPO) provide useful quantitative information but are invariably destructive, although more recently, technique developments in XRD[6] and combined ^{13}C NMR-TGA[7] have begun to provide further insight into the role of carbonaceous deposits in catalyst deactivation and methane dehydroaromatisation mechanisms. Vibrational spectroscopy methods such as Raman and IR spectroscopy provide detailed fingerprint information on speciation but are often convoluted by a strong fluorescence background, particularly with increasing temperature[8]. This is often the case when organic products begin to form in catalytic reactions or when coking starts to occur[9]. Although gating systems exist to remove the background, these have limited effectivity and are often complex and costly[10].

Instead of considering this fluorescence emission as an unwanted signal to be subtracted out as a background, it is possible to analyse light emission from fluorophores that proliferates naturally throughout the course of a catalytic reaction as a signal in its own right. Photoluminescence (PL) in zeolites is a well-recognised phenomenon that has been attributed to various sources. Some studies such as those by Liu et al. who recorded the emission from SDA in zeolite structure ITQ-

26[11] and a prolific body of work by Hashimoto et al.[12] focus the interpretation of emission spectra on the presence of adsorbed organic species. The effect of metal loading on PL spectra has also been previously acknowledged in studies on copper species[13,14,15], silver clusters[16], lanthanoid complexes[17], manganese doping[18], and europium exchanged frameworks[19], as well as non-metallic sulphide clusters[20]. Studies also exist that focus on PL emission of the framework itself such as Planells et al. and their work on PL in crystallised silicalite-1 films[21] and Wang et al. in their work on zeolite derived glasses, which attribute PL to an ordered-disordered transition[22-23]. Theoretically, studying PL is an excellent way to gain further insight into the adsorbed organics residing within the complex internal landscape of zeolite microstructures because it directly pertains to molecular-level processes of energy absorption and emission. Subsequently, changes in emission lifetime and spectral peak positions can be linked to guest molecule behaviour and numerous non-intrinsic material properties such as different non-radiative decay pathways, energy transfer, and intersystem crossing, all of which may be influenced by environmental factors.

In this paper, time-resolved photoluminescence spectroscopy (TRPS) has been identified as an alternative complementary means of analysing carbonaceous species in catalysis. TRPS is an established non-destructive spectroscopy technique that uses laser excitation to induce characteristic photoemission from a sample[24]. Using an intensified camera and a pared back optical geometry, fluorescence and phosphorescence information can be detected with a high degree of sensitivity. Although traditional steady-state fluorescence measurements often yield broad, relatively featureless spectral profiles with limited chemical specificity, TRPS features the addition of a time gate to the detection system, which imparts datasets with an enhanced capability to differentiate emissive components within the sample. Analysis can, therefore, be conducted in two directions, namely temporal or spectral, with the possibility to visualise data by either time-gated spectra, decay profiles in specific spectral regions, or simultaneously in both. The use of a UV-laser makes the system well-placed to specifically probe volatile organic species.

The purpose of this study is to demonstrate the capabilities of TRPS when analysing adsorbed organics in zeolites, and to demonstrate how this technique could be applied to more complex systems in the future. For this reason, a controlled detemplation of an industrially relevant chabazite (CHA) topology zeolite was selected. To ensure stable crystallisation during the synthesis process, commercial zeolites are commonly manufactured with organic structure directing agents (OSDA), the commonest of which are typically amine or alkyl cations. The OSDA, which is not integral to the zeolite's catalytic functionality, is decomposed and removed from the framework via a thermal calcination process called detemplation. Characterisation of the carbogenic species formed during detemplation have previously been attempted using UV-vis & fluorescence microspectroscopy[25] and positron annihilation lifetime spectroscopy[26], with both studies focusing on MFI-type zeolites. In this paper, a comparative study between three zeolite samples quenched at different stages of the calcination procedure (i.e. an uncalcined, a partially calcined, and a fully calcined chabazite zeolite) was conducted. Electing to focus on detemplation should not misrepresent the broader applicability of this technique, which could potentially provide novel insight into the nature of adsorbed phases of other catalytic systems such as the methanol-to-olefins reaction, methane dehydroaromatisation, or even mechanisms of coke poisoning.

In the first section, the PL spectrum of the OSDA N,N,N-trimethyl-1-adamantylammonium hydroxide (TMAda) was established, and subsequently probed in the uncalcined sample. A focus was placed on the confinement effects guest molecules experience when trapped inside chabazite's characteristic cage-channel structure. In the second section, gated spectra are used to highlight the similarities and differences between PL spectra of an uncalcined and a partially calcined zeolite.

In the third section, a comparison between an uncalcined and a calcined zeolite show that gated spectra and lifetime analysis can track the depletion of TMAda molecules. By studying lifetime components discernible in different spectral regions, it was possible to attribute certain spectral variations to the steric effects of occlusion, and other variations to the formation of new combustion species that disappear following a full calcination. In studying the long-lived microsecond range, phosphorescent signatures attributed to the presence of occluded template were recorded.

2. EXPERIMENTAL SECTION

Zeolite Background. Chabazite is a triclinic crystal, noted for its unique network of cages connected by narrower channels (see Figure 1A). Structure-wise, it is a well-known member of the ABC 6-family of zeolites, comprised of a stacked sequence of 6-rings arranged to form double 6-rings at the apices of its rhombic unit cell. The eight ringed cages have an aperture of roughly 3.8 x 3.8 Å[27]. The largest internal cage diameter is 8 Å, and the pore limiting diameter is 4.2 Å. Trimethyladamantammonium hydroxide is a quaternary ammonium hydroxide (see Figure 1B).

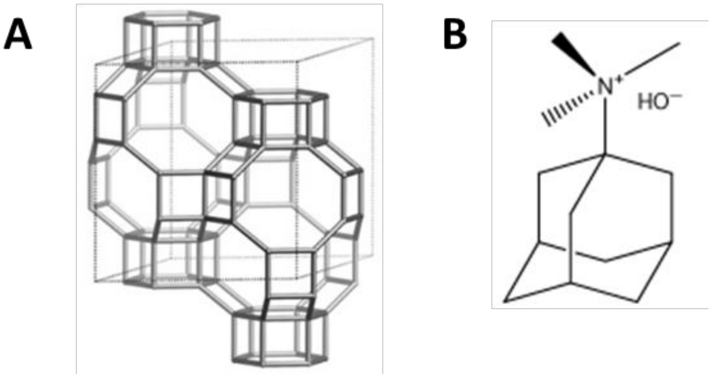

Figure 1 (A) Chabazite-type zeolite structure[28] and (B) trimethyladamantylammonium hydroxide (TMAda) structure

Sample Preparation. Four samples were analysed in this study: template material, uncalcined chabazite, calcined chabazite, and a chabazite sample quenched halfway through the calcination process. Template material was measured in solution form and comprised 25 % TMAda and 75 % water (Sachem).

Template stabilised SSZ-13 zeolite (Si/Al = 15) was synthesised as described previously under hydrothermal conditions[29] with TMAda (Sachem) as the organic structure directing agent. As-made zeolite was dried overnight in air at 80 °C to form a white powder that was stored in glass vials under atmospheric conditions. This dried sample is termed the 'uncalcined sample'. A portion of the as-made zeolite was subjected to a standard calcination procedure. This involved placing the sample in a ceramic dish in a static oven and heating in air to 120 °C at 1 °C/min and holding it at this temperature for 2.5 h, then heating it further, to 550 °C at 4 °C/min and holding at this temperature for 10 h to create the calcined sample. [30] The intermediate sample was synthesised by observing the same calcination conditions but quenching the sample after completion of the temperature ramp to 550 °C.

Theoretical Calculations. A combined Monte Carlo-Simulated Annealing procedure is used to determine low energy sites for the TMAda template molecule in the CHA framework. The calculations were run using the Sorption and Forcite modules within Materials Studio 2017[31]. The COMPASS forcefield[32] was used to describe all zeolite-template interactions. The Monte Carlo part of the calculations was used to locate possible sites for the sorbate molecule within the zeolite structure. The CHA framework was optimised prior to the Monte Carlo simulation. During the Monte Carlo simulation both the zeolite framework and the template molecule are assumed rigid, which results in a strained system. To find the global minimum a simulated annealing procedure was used on the lowest energy configurations obtained from the Monte Carlo simulations where the framework, template, along with the cell parameters were optimised. The zeolite framework was assumed to be siliceous and the balancing charge accounted for by scaling the charges on the framework atoms[33]. The charges used in the simulation are given in Table 1.

Table 1 Atomic charges for simulation

Atom	**q (esu)**
Si	+0.862
O	-0.445
C attached to N and methyl group	0.248
C attached to N and C	0.407
sp3 C	-0.106
C with 3 C neighbours	-0.053
H	0.053
N	-0.628

Raman Spectroscopy. Raman spectra were obtained from an InVia confocal Raman microscope equipped with a 50x objective lens (Nikon, L Plan Apo, 50x/0.45, WD17) and Peltier cooled CCD. Sample was irradiated with either an 830 nm diode laser with 500 mW maximum power output, or a 514 nm argon laser (Stellar PRO, Modu-laser) with 50 mW maximum power output. A grating with 1200 lines/mm was used. Attenuated power at the sample is achieved using neutral density filters.

Time-Resolved Photoluminescence (PL) Spectroscopy and Data Analysis. The time-resolved fluorescence spectroscopy setup used is a variation of the Q-switched laser & gated camera setup previously described by Dozzi et al.[34]. Powdered samples were flattened on an aluminium plate and liquid samples were measured in a quartz cuvette. The sample surface was irradiated at a 45° angle with the 355 nm third harmonic of a pulsed Nd:YAG (CryLas FTSS 355-50, Crylas GmbH, Berlin, Germany). The system works at low rep rate of 100 Hz with a laser pulse width of 1 ns, allowing us to measure the lifetime of both permitted singlet transitions in the nanosecond regime and dipole forbidden triplet transitions in the microsecond or millisecond regime. A low power density of 0.9 μW/cm^2 was used. A mirror was placed above the sample at 45° to step the emitted signal (375 – 750 nm) onto a simple optical system comprised of two lenses (Ø 1 inch, f = 100 mm) that focused the light onto the slit of an Acton SP-2300i spectrometer (focal length = 300 mm, f/4 aperture) matching its aperture. Signal was detected with a high-speed image intensifier (C9545-03, Hamamatsu Photonics, Japan) and CCD camera (Retiga R6, Q-imaging, Canada). The image intensifier provides a minimum gate time of 3 ns and a variable amplification factor. The CCD camera is coupled to the image intensifier by a lens system. The detector was fully characterized in terms of spectral sensitivity, photometric gain and temporal response before the experiment. A delay generator (DG535, Stanford Research Systems, Sunnyvale CA, USA) and homemade circuit based on a fast photodiode coupled to a constant fraction discriminator were used to synchronise the laser pulses and gated intensifier. The overall RMS jitter of the detection system was below 500 ps, which sets the accuracy of lifetime measurements below 1 ns.

Data were collected in three modes. The first mode was ‘quasi-CW spectra’, where the gate width on the intensifier was set to 150 ns synchronous with the laser pulses for fluorescence regime CW, and to 5 ms with a 10 μs delay capturing the CW spectrum of any longer-lived phosphorescent components. For fluorescence, a gate much longer then its average decay time was used to capture almost all the signal, while removing the ambient light and reducing the electronic noise; for phosphorescence, the gate was required to remove the short living emission. The second mode was 'gated spectra', where the gate width was set to 10 ns and a series of delayed spectra were acquired every 10 ns, starting from a 0 ns delay with respect to the laser pulses. This was to ensure no temporal overlap between the spectra measured. Finally, 'lifetime measurements' were acquired by setting a gate width of 10 ns and acquiring a series of delayed spectra at varying delays *d*. To optimise the fit, spectra were sampled more heavily in the early portion of the decay curve immediately following excitation. Uneven temporal sampling was adopted to account for the different decay times of the emission components. Each lifetime dataset was analysed across specific spectral regions, as defined in the results section. The spectral elements of each interval were summed to give spectrally resolved decay curves, which were fitted independently to a multiexponential model function to recover the amplitude and lifetime of two or three emission components.

The model function is:

$$F(d) = \sum_{i=1}^{N} A_i \tau_i \left(1 - e^{-W/\tau_i}\right) + W \cdot Offset,$$

where F is the total fluence, i.e., the integral of the emission intensity within the gate window, d is the acquisition delay for each time point of the sequence, while Ai and τ_i (i = 1, 2, 3) are the amplitude and lifetime of the emission components. The term $[1 - \exp(-W/\tau_i)]$ is required to correct for the finite width (W) of the sampling window (10 ns). The fitting method was based on a standard least mean square algorithm derived from the math library provided by the Numerical Algorithms Group (NAG).

3. RESULTS & DISCUSSION

Defining Organic Products Present During Detemplation. To highlight the capability of TRPS, detemplation of chabazite was selected due to the relative predictability of the organic products present within the zeolite framework at different stages in the detemplation process. Following synthesis, uncalcined chabazite appears white to the naked eye (see Supplementary 1A). Prior to the calcination procedure, TMAda molecules are contained within the cages of the framework. Template molecules for chabazite framework are large relative to the cage size. Energy minimised modelling (see Figure 2) reveals that a maximum of one template molecule may occupy a single cage. Shown to be highly spatially restricted and only able to sit in one alignment within the cage volume, there is no scope for multiple TMAda molecules to occupy a single cage. This means that in this uncalcined zeolite system, we do not expect to see significant TMAda molecule-molecule interactions such as excimer formation, which has been postulated in zeolite studies of adsorbed organics to augment PL lifetime dynamics[35,36,37].

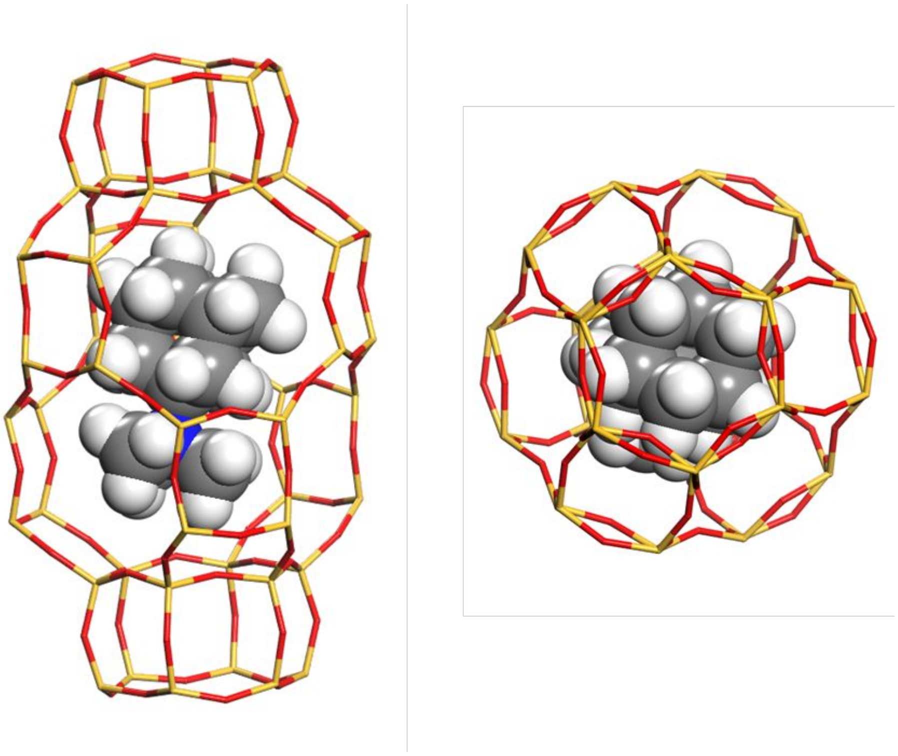

Figure 2 Energy minimized optimized structure of TMAda inside a chabazite cage

During the calcination process, the zeolite sample begins to discolour and darken (see Supplementary 1B). This is as a result of the proliferation of bulky template combustion derivatives and coke[38]. At this stage it is expected that a mixture of template molecules and calcination products will be present in the zeolite. Following the calcination process, the sample returns to being white (see Supplementary 1C). It is expected that whole template molecules will no longer remain following an extended thermal treatment process and given the colour change of the sample it is unlikely that significant amounts of coke remain however it is possible that trace amounts of smaller template combustion derivatives may be present.

The presence of TMAda in uncalcined chabazite was confirmed using Raman spectroscopy (see Figure 3). Specifically, the bands in uncalcined chabazite at 777, 800, 941, 977, 985, 1103, 1200, 1283, 1305, 1368, 1444, and 1452 cm^{-1} display agreement with the template spectrum and can be attributed to C-C stretching and H-C-C bending of the adamantane structural base unit[39]. Following calcination, these bands are no longer visible, implying that whole TMAda molecules are no longer present following the thermal treatment. Residual in the calcined chabazite are a double peak at 466 & 484 cm^{-1} and at 803 and 831 cm^{-1}. The band at 466 cm^{-1} is dominant in the calcined chabazite sample and is well established as the class A vibration of the SiO_2 unit cell[40,41] and the 484 cm^{-1} is characteristic to the chabazite framework. The bands at 803 and 831 cm^{-1} are assigned to weaker symmetric v_s(T-O-T) stretches[42,43] of the framework. There are no obvious D or G bands associated with graphitic carbon structures, so it is likely that the hydrocarbon speciation present is predominantly molecular. Characteristic Raman spectra showing template fingerprint or molecular combustion derivative peaks could not be obtained from the partially calcined chabazite using conventional 514 nm or 830 nm Raman spectroscopy due to the high fluorescence background. However, an alternative method of Kerr-gated Raman (see Supporting 2) shows a D and G band confirming the presence of amorphous and graphitic carbon structures as part of the coke build-up.

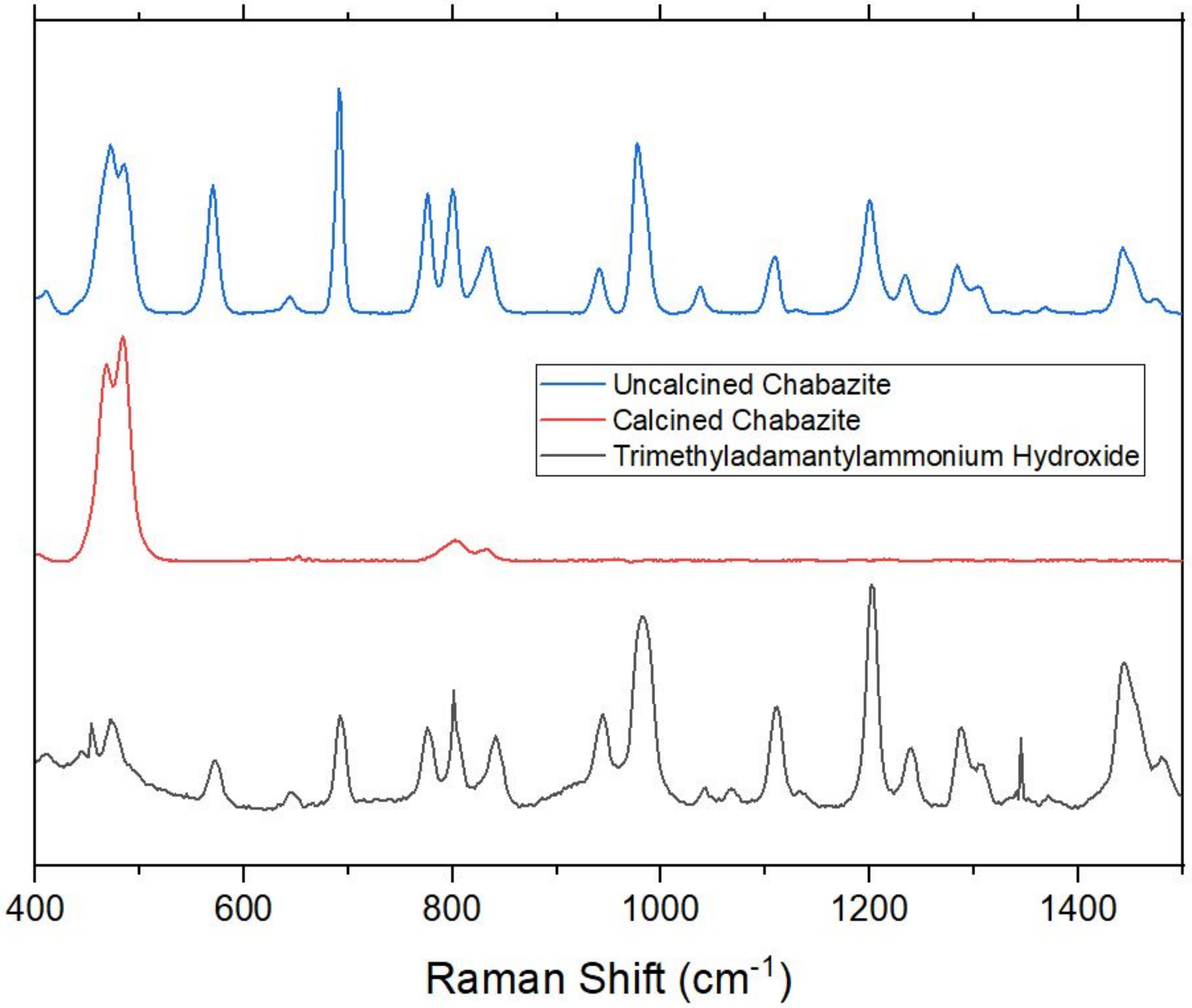

Figure 3 Raman spectra at 830 nm 250 mW excitation of synthetic uncalcined chabazite (blue), calcined chabazite (red), and 514 nm 25 mW excitation of OSDA (black) acquired with 1200 l/mm

Effect of Confinement on Template Emission Inside Zeolite Pores. In the following section, the emission behaviour of TMAda is established and then compared with the emission behaviour of an uncalcined, template-laden chabazite sample. The discussion surrounding this comparison is focused on how the emission behaviour of TMAda changes when it is confined within the pores of a zeolite.

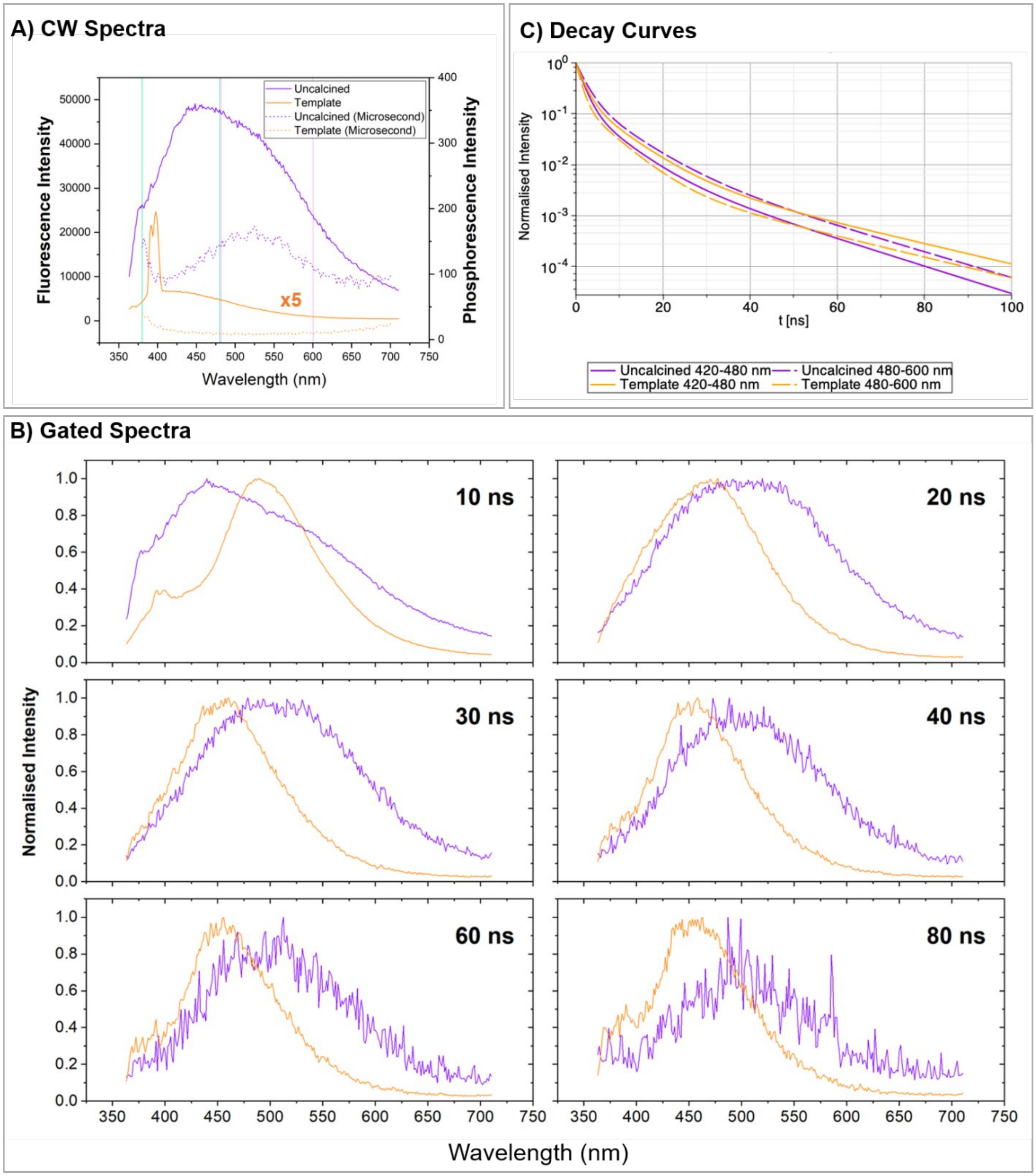

Figure 4 Comparison of TRPS ensemble data for uncalcined zeolite and template. A) Continuous wave spectra of uncalcined zeolite (purple) and template (orange) fluorescence emission in solid line and phosphorescence emission in dotted line, B) Gated spectra of uncalcined zeolite (purple) and template (orange) at 10 ns gate intervals C) Lifetime analysis in two spectral regions (417-480 nm and 480-600 nm) with decay curves.

Table 2 Table of lifetimes and amplitudes in two spectral regions (417-480 nm and 480-600 nm)

Sample	Wavelength Range (nm)	A_1%	A_2%	A_3%	τ_1	τ_2	τ_3	$A_1\tau_1$%	$A_2\tau_2$%	$A_3\tau_3$%	τ_{Av}
Template	417-480	0.79	0.20	0.01	1.6	6.5	21.8	46.1	45.3	8.6	5.6
	480-600	0.83	0.16	0.01	1.1	5.6	21.2	47.4	45.3	7.3	4.6
Uncalcined	417-480	0.84	0.14	0.01	1.6	5.9	16.2	55.1	35.2	9.7	4.5
	480-600	0.77	0.21	0.02	2.0	6.7	17.3	47.2	42.3	10.5	5.6

The CW fluorescence and phosphorescence emission spectra of TMAda and uncalcined chabazite are presented in Figure 4A. TMAda has a significantly lower emission intensity than uncalcined chabazite. This can be explained by the fact that uncalcined chabazite is a highly scattering powder, whereas TMAda is measured as a liquid being in solution with water. High levels of scattering in the powder produce a large increase in the laser intensity in the superficial layer of the sample as the photons repeatedly bounce back and forth before being either absorbed or reflected. Similarly, the solution form of TMAda is likely to experience quenching as the fluorescence intensity and lifetime are influenced by the solvent polarity and viscosity, and by the concentration.

The CW spectrum of TMAda features a broad emission curve peaking at 420 nm, with a sharp double peak at 388 nm and 396 nm. The double peak is ascribable to a Raman signature. The 396 nm peak is equivalent to the Raman band of O-H for water at 3400 cm^{-1}, which is further confirmed by a variable excitation wavelength study where the peak position shifts accordingly with respect to the excitation wavelength[44], and the 388 nm band (equivalent to a 2395 cm^{-1} Raman shift) is likely a C-H stretch Raman peak associated with the template material. The instantaneous nature of these bands, which appear at a time on par with the response function of the TRPS system, is evident in the gated spectra (see Figure 4B) where the bands are no longer visible from the second time gate onwards and are consistent with their Raman origin. The CW spectra of uncalcined zeolite is a broad fluorescence emission profile with a peak at 450 nm and a broad shoulder appearing from 540 nm onwards. When a millisecond gate was applied, phosphorescence signal from the template was no longer observable. However, uncalcined chabazite exhibits a phosphorescence signal with a peak at 525 nm. A more extensive analysis of the phosphorescence is included further on in Figure 6.

Time gating makes it possible to decouple the Raman contribution from true photoluminescence signal in the template material. In gated spectra measurements (see Figure 4B), it is possible to see that TMAda has two different spectral profiles. In the first window, the fluorescence profile has a peak at 490 nm, whereas from 30 ns onwards the peak is at 450 nm. At 20 ns the peak appears to be at an intermediate position at 470 nm. Rather than a peak shift, this suggests that TMAda has two primary emissive components with different lifetimes that combine to form different profiles at different time gates. The first gate, therefore, shows a fast-living component that appears to have predominantly disappeared after 30 ns, as the emission spectrum from this time-gate onwards is centred around 450 nm.

Similarly, the uncalcined chabazite's broad fluorescence emission curve also changes across different time windows. The dynamic appears more complex than the TMAda alone, and there are at least two discernible components. The first component can be seen clearly in first time gate where the profile looks similar to the CW spectrum but with the peak at 440 nm appearing more pronounced. This means the CW spectrum is being dominated by fast-living species that decay within the first 10 ns. The second component is visible from the second time gate onwards where the spectrum is centred around 500 nm. There are also visible differences in the full width half maxima (FWHM) of the spectrum at 20-30 ns compared to 50 ns onwards, implying there is likely contribution from a complex of other fluorescence components. The use of time-resolved spectra enables the identification of TMAda's two primary components and demonstrates that the second component instead appears to red-shift from 450 nm to 500 nm upon confinement.

Based on the emission dynamic visible for both samples in the gated spectra, two spectral regions were selected for lifetime analysis. 417-480 nm was selected to capture both the longer-living component in the TMAda and the fast component in the uncalcined material, and 480-600 nm was selected to separate out the uncalcined material's longer-living component. Both samples were fit to a triexponential function. As indicated from the gated spectra, the fluorescence amplitude of τ_1 is the greatest for both samples in both spectral regions. In the spectral region 417-480 nm, the lifetimes are all shorter in the uncalcined sample with a τ_{av} of 4.5 ns versus 5.6 ns in the template. However, a lengthening of τ_1 & τ_2 is seen in the spectral region 480-600 nm, where $\tau_1 = 1.1$ ns & $\tau_2 = 5.6$ ns for the template and $\tau_1 = 2.0$ ns & $\tau_2 = 6.7$ ns for the uncalcined chabazite. Although in this temporal domain τ_3 is shorter in this region for the uncalcined chabazite, this sample also exhibits a microsecond length phosphorescent component not present in the template material.

Overall, in this spectral region there is a significant increase in emission lifetimes. This is coupled with an increase in fractional amplitude values for τ_2 & τ_3 in this region ($A_2\%$, $A_3\% = 0.20$, 0.02 for uncalcined chabazite; and 0.16, 0.01 for template), highlighting an interesting change in emission dynamics when TMAda is confined within the framework structure. It is postulated that confinement reduces permutations for steric conformation and by extension self-quenching of the TMAda leading to an extended triplet state lifetime and greater intersystem crossing efficiency. Room temperature phosphorescence (RTP) of TMAda has been previously reported by Ramamurthy et al.[4546] who suggest that cationic sites in zeolites may induce singlet-triplet spin conversion in molecules. Casal et al.[47] also observed an increase in the lifetime of β-phenylpropiophenone at room temperature in silicalite, attributing an increased stability of the triplet state to steric confinement within the channels.

It is known that zeolite samples have complex photoluminescence mechanisms that have variably been attributed to composition[48], metal loading[14] or metals stabilised inside a matrix[49], and product formation[25] in previous studies. It has been assumed here that in the case of uncalcined chabazite, a significant proportion of the emission is arising as a result of the photoemissive excitation of TMAda. The assumption does not discount contribution from other emission pathways. Indeed, uncalcined zeolite systems offer an interesting model for studying the confinement effects of a crystalline lattice on photoexcitable molecules. Although photoluminescence studies on confinement effects exist where highly emissive molecules are floated into zeolite pores[37] and monitored for changes in spectral profiles, a host of problems often arise during the sample preparation process that critically hamper deeper interpretation of results, including surface aggregate formation and crystallisation[12]. These are problematic in that they no longer represent a measurement from a sample with evenly distributed, geometrically confined fluorophores. Further to this, the size discrepancy between the host cages and adsorbent molecules poses as a double-edged sword; zeolite channels need to be large enough (or adsorbent molecules small enough) to achieve confinement of introduced molecules in the first place, but the sites of entrapment may not be restrictive enough to induce effects of electronic orbital deformation on the molecules. The OSDA is an ideal candidate for observing changes in emission properties due to confinement effects as they are distributed more evenly throughout the sample and represent the upper size limitation for molecules that can be accommodated within a zeolite cage, and by extension experience a significant degree of steric and electronic confinement. In the case of chabazite, the TMAda acts to template the cage portion of chabazite's cage-channel structure and would be impossible to retrospectively introduce a molecule of this size into the pores due to the size selectivity of the channel diameters.

Proliferation of Carbonaceous Deposits in Part-Calcined Sample. Size selectivity of chabazite channels necessitates the decomposition of bulky TMAda molecules into smaller before pores can be successfully evacuated. When colour changes become discernible to the naked eye, it is a reasonable indication that coke has begun to build up on the zeolite sample.

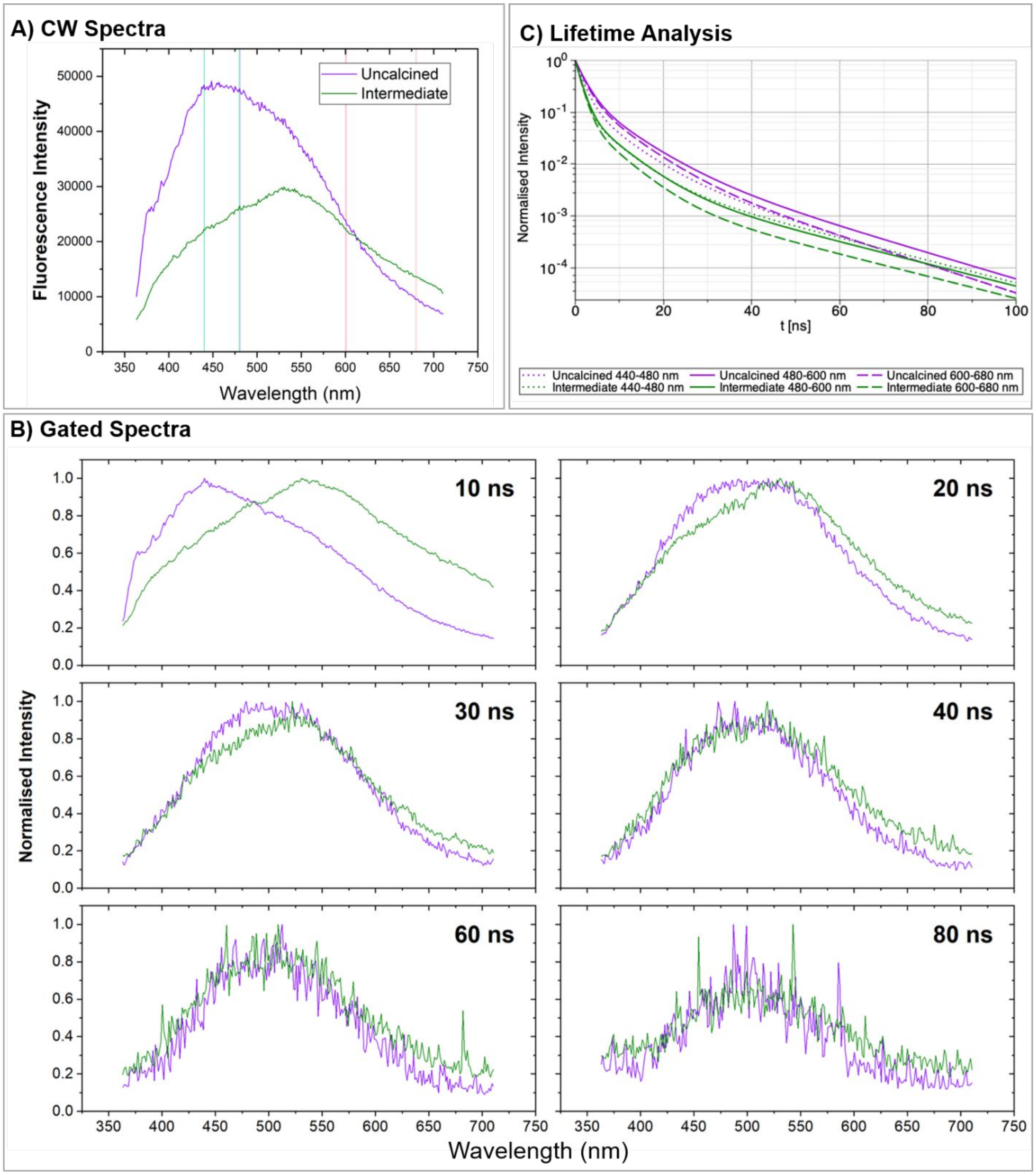

Figure 5 Comparison of TRPS fluorescence ensemble data for uncalcined zeolite and intermediate zeolite. A) Continuous wave spectra of uncalcined zeolite (purple) and intermediate zeolite (green) fluorescence emission in solid line and phosphorescence emission in dotted line, B) Gated spectra of uncalcined zeolite (purple) and intermediate zeolite (green) at 10 ns gate intervals C) Lifetime analysis in three spectral regions (440-480 nm, 480-600 nm and 600-680 nm) with decay curves

Table 3 Table of lifetimes and amplitudes in three spectral regions (440-480 nm, 480-600 nm and 600-680 nm)

Sample	Wavelength Range (nm)	A_1%	A_2%	A_3%	τ_1	τ_2	τ_3	$A_1\tau_1$%	$A_2\tau_2$ %	$A_3\tau_3$%	τ_{Av}
Uncalcined	440-480	0.82	0.16	0.02	1.6	5.8	15.9	0.52	0.37	0.11	4.8
	480-600	0.77	0.21	0.02	2.0	6.7	17.3	0.47	0.42	0.11	5.6
	600-680	0.77	0.21	0.02	1.9	6.3	15.9	0.48	0.43	0.09	5.0
Intermediate	440-480	0.88	0.11	0.01	1.2	5.6	20.1	0.58	0.34	0.08	4.2
	480-600	0.89	0.11	0.01	1.3	5.9	20.4	0.61	0.33	0.06	4.0
	600-680	0.91	0.08	0.00	1.3	5.6	20.4	0.68	0.27	0.04	3.3

CW spectra in Figure 5A show that the intermediate zeolite has a peak at 540 nm, and an emission intensity lower than the uncalcined sample. The CW emission intensity of this sample is neither directly comparable with the uncalcined sample nor representative of the concentration of fluorophore molecules present as it is significantly darker and likely to be reabsorbing some of the emission.

Gated spectra in Figure 5B show that the intermediate sample has a fast component present with a peak at 540 nm in the first 10 ns window that heavily influences the profile of the CW spectrum. This faster component, which so far appears characteristic to the intermediate sample is attributed to the proliferation of new hydrocarbon products. The difference in peak position between the uncalcined material at 440 nm and the intermediate sample at 540 nm implies there has been a dramatic change in the speciation of fast emitting components following a thermal treatment.

From 40 ns onwards, the gated spectra show that the intermediate and uncalcined samples exhibit a significant degree of similarity. The component visible in the uncalcined sample from 40 ns onwards was assigned to the presence of the occluded template molecules. Detection of this signal in the intermediate sample suggests that whole TMAda molecules are still present after 6 hours of ramping the sample up to 550 °C under air flow. Comparisons between the uncalcined and the intermediate sample serve as worthwhile examples of how pulling apart the temporal aspect of an emission spectrum can be very useful in systems with complex origins of emission. In both samples, it is evident that fast components, which can vary hugely in concentration and composition across a sample, may cloud the interpretation of CW spectrum. Probing different time windows makes it possible to discern how template molecules and combustion by-products co-exist alongside each other, each with different local microenvironmental influences.

Lifetime analysis was conducted in three spectral regions: 440-480 nm, which captured the fast component of the uncalcined sample; 480-600 nm, which was selected as the probe region for occluded TMAda as per the previous section; and 600-680 nm, which covers the tail of both curves. A triexponential fit was used.

Although a strong visual correlation between the uncalcined and intermediate samples in the gates from 40 ns onwards exists, the lifetime analysis in the template probe region of 480-600 nm shows differences in τ values. In the intermediate samples τ_1 and τ_2 become shorter, with the fractional amplitude of the faster component τ_1 increasing with respect to τ_2 (i.e. $A_1\% = 0.89$, $A_2\% = 0.11$ in intermediate zeolite; $A_1\% = 0.77$, $A_2\% = 0.21$ in uncalcined zeolite), relating to the overall decrease in whole TMAda molecules in the intermediate sample and the proliferation of new hydrocarbon species. Although having a lower percentage amplitude than the uncalcined sample, the τ_3 of the long-living components in the intermediate samples are markedly longer (20 ns vs. 15 ns) across all spectral regions. In the long wavelength region (480-600nm) we observe a significant reduction in the average lifetime of the intermediate (τ_{Av} = 3.3 ns) sample with respect to the uncalcined sample (τ_{Av} = 5.0 ns). This confirms that the emission in this band is dominated by reaction products that, being likely small organic molecules, exhibit fast relaxation dynamics. This is well represented in Figure 5C, where the fastest fluorescence decay is that of the intermediate sample in the third band. It is expected that the template derivatives present in the intermediate sample, being smaller and capable of travelling along size-selective diffusion pathways, will have a greater freedom of distribution across the crystals, with some remaining in the centre following quenching and others residing towards the surface[50]. By extension, not all combustion products will necessarily experience the degree of steric confinement imposed upon the TMAda molecules, opening up a wider range of possibilities of lifetime states one might expect to see.

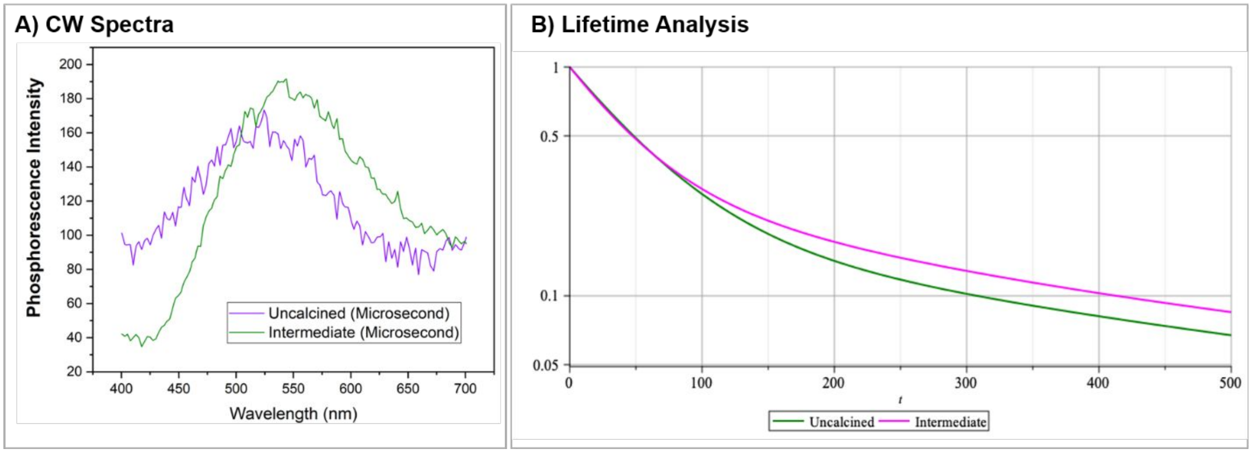

Figure 6 Comparison of TRPS phosphorescence ensemble data for uncalcined zeolite and intermediate zeolite. A) Continuous wave spectra of uncalcined zeolite (purple) and intermediate zeolite (green) fluorescence emission in solid line and phosphorescence emission in dotted line, B) Lifetime analysis in one spectral region (480-600 nm) with decay curves and table of lifetimes and amplitudes.

Table 4 Fractional amplitude and lifetime values for phosphorescence measurements in uncalcined and intermediate samples

Sample	A_1%	A_2%	A_3%	τ_1	τ_2	τ_3	$A_1\tau_1$%	$A_2\tau_2$%	$A_3\tau_3$%	τ_{Av}
Uncalcined Phosphorescence	0.80	0.10	0.10	53.1	239.5	811.3	0.28	0.17	0.55	368.0
Intermediate Phosphorescence	0.69	0.18	0.13	44.3	185.4	840.7	0.18	0.19	0.64	356.8

Both the uncalcined and intermediate zeolites exhibit measurable phosphorescence behaviour. The CW spectra in Figure 6A show that the intermediate sample peaks at 545 nm and the uncalcined sample peaks at 520 nm. Lifetime analysis was conducted across the entire spectral region, and triexponential fits were used. Even if data are rather noisy due to the scarcity of photons in the long tail of the emission, a tentative lifetime fit could be done also for the phosphorescence dataset (Figure 6B). It may be noted that in the leading edge of the fitted curves uncalcined and intermediate behave in a similar way, with the intermediate displaying a slightly slower damping before reaching the same slope (i.e. lifetime) of the uncalcined in the long term. Notwithstanding some caution in drawing conclusions from a non-completely reliable dataset, it could be speculated that the same triplet states of TMAda, which might be the origin of the phosphorescence in the uncalcined sample, are also present in the intermediate sample with the possible existence of additional long emitting compounds.

Depletion of Template Signature from Uncalcined to Calcined Sample. In the final section of this discussion, the depletion of template material is monitored in a comparison of uncalcined and calcined chabazite. Immediately discernible differences are visible in the CW spectra (see Figure 7A), where the calcined sample, when compared to the uncalcined sample, appears to have a generally simpler, Gaussianesque spectral profile centred around 410 nm. The peak intensity is also over two times lower than the uncalcined sample. Gated spectra in Figure 7B highlight the simpler emission dynamic of the calcined material, with minimal changes occurring between the 10 ns and 20 ns windows when compared to the uncalcined material. Compared to the uncalcined material, all gated spectra of the calcined material show a marked decrease in luminescence activity in the red region (i.e. from 480 nm onwards). Although the normalisation in Figure 7B effectively shows the contrast in peak positions, the CW spectra comparison in Figure 7A more accurately highlights the large discrepancy in emission in this region. This is directly attributable to the depletion of whole TMAda molecules and the majority of coke products, which appear broadly to have been removed as demonstrated by previous Raman measurements (see Figure 3) and the white sample colour. The loss of phosphorescent signal in the calcined sample is compatible with the depletion of TMAda and further supports the notion that the phosphorescence exhibited in the uncalcined and intermediate samples in synthetic zeolites pertains to occluded hydrocarbon material rather than arising from the framework itself. Phosphorescent lifetimes can be easier to fit than multiexponential fluorescence lifetimes that require more refined sampling around time zero. This enhanced component separation makes phosphorescent signatures ideal for flagging the presence of templating material. In future work, this approach may be utilised in *in-situ* detemplation monitoring.

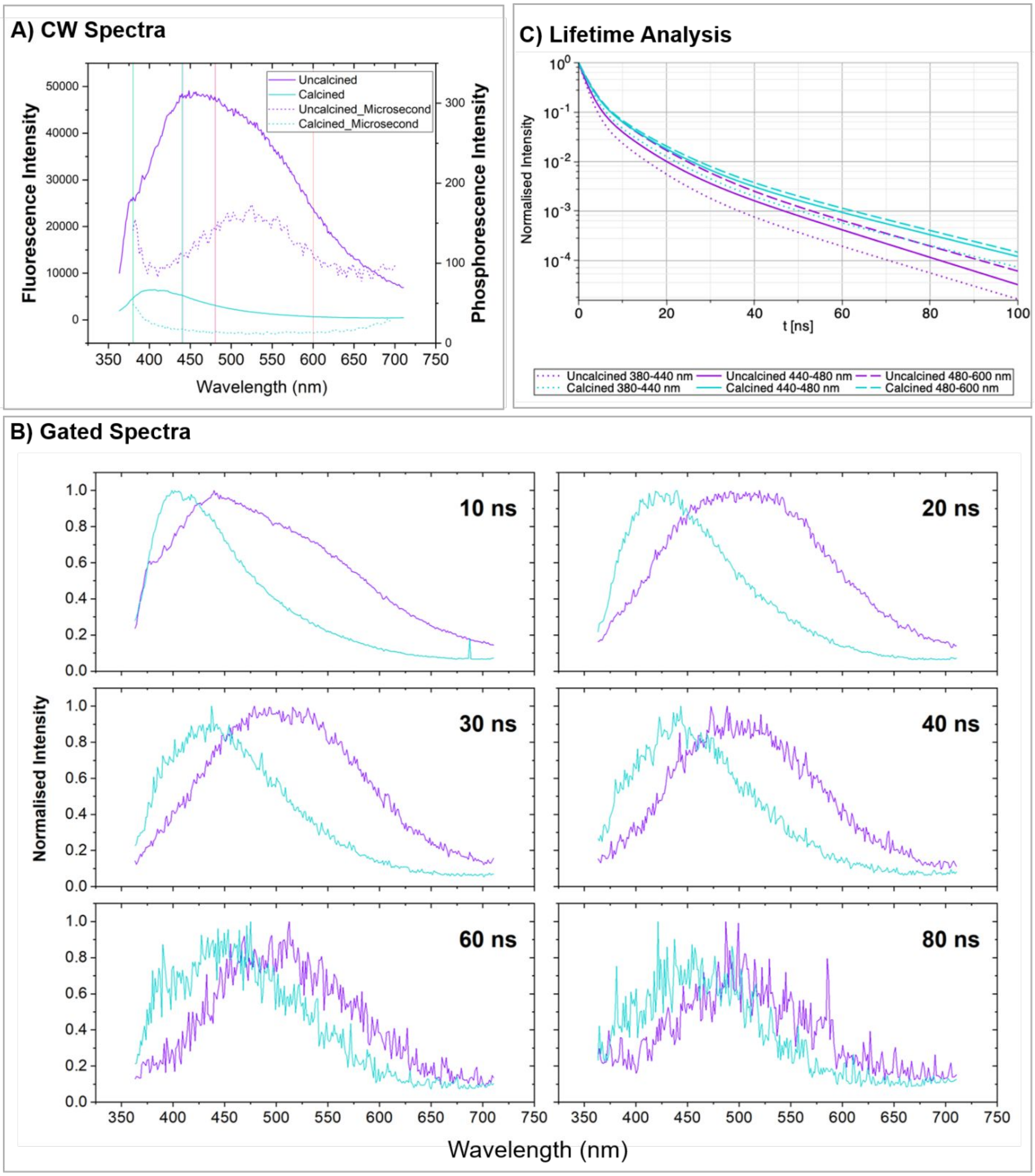

Figure 7 Comparison of TRPS ensemble data for uncalcined zeolite and intermediate zeolite. A) Continuous wave spectra of uncalcined zeolite (purple) and calcined zeolite (pink) fluorescence emission in solid line and phosphorescence emission in dotted line, B) Gated spectra of uncalcined zeolite (purple) and calcined zeolite (pink) at 10 ns gate intervals C) Lifetime analysis in three spectral regions (380-440 nm, 440-480 nm and 480-600 nm) with decay curves

Table 5 *Table of lifetimes and amplitudes in three spectral regions (380-440 nm, 440-480 nm and 480-600 nm)*

Sample	Wavelength Range (nm)	A_1%	A_2%	A_3%	τ_1	τ_2	τ_3	$A_1\tau_1$%	$A_2\tau_2$%	$A_3\tau_3$%	τ_{Av}
Uncalcined	380-440	0.89	0.10	0.01	1.5	5.9	16.4	0.65	0.29	0.06	3.7
	440-480	0.82	0.16	0.02	1.6	5.7	15.7	0.51	0.37	0.12	4.8
	480-600	0.77	0.21	0.02	2.0	6.7	17.3	0.47	0.42	0.11	5.6
Calcined	380-440	0.83	0.15	0.01	1.9	6.9	19.8	0.55	0.37	0.08	5.2
	440-480	0.78	0.21	0.02	1.9	6.9	19.8	0.45	0.43	0.11	6.1
	480-600	0.77	0.21	0.02	1.9	7.1	19.8	0.43	0.43	0.13	6.5

Lifetime analysis was conducted in three spectral regions: 380-440 nm, which again captured the fast component of the calcined sample; 440-480 nm; and 480-600 nm, which is the probe region for the template. A triexponential fit was used. Compared to the uncalcined sample, the τ values in the calcined sample are virtually identical across all spectral ranges, giving an average of τ_1 = 1.9 ns, τ_2 = 7.0 ns, τ_3 = 19.8ns. A notable difference in the calcined sample is the fractional amplitude values in the spectral region 380-440 nm, which has a greater contribution from A_1% and less from A_2% when compared to the two other spectral regions. This means that the region 380-440 nm is generally faster than the regions 440-480 and 480-600 nm, where longer-lived components have a slightly greater bearing in the overall composition of lifetimes. In comparing the uncalcined sample with the calcined sample, the lifetimes in the calcined sample are longer for all three components across all three spectral regions with the exception of τ_1 in region 480-600 nm of the calcined sample, which is 0.1 ns shorter than the uncalcined sample. It should be noted that the significantly decreased signal in this region for the calcined sample makes meaningful lifetime fitting more challenging. The global increase of lifetimes here would be consistent with the depletion of contribution from occluded hydrocarbons, which are shown to have a faster lifetime. Coupled with the depletion of phosphorescence, which was previously flagged as an alternative way of tracking the presence of occluded template, this lengthening of lifetimes can be used to show that TRPS is capable of detecting the presence of OSDA but even further decouple the original OSDA emission from an additional PL signal.

Based on this, it is possible to speculate the emission source in the calcined zeolite originates primarily from a single type of fluorophore that experiences different quenching effects, with the multiexponential fit correlating to different relaxation pathways. In this case, variations visible in the decay curves as presented in Figure 7C can be justified assuming the fluorophore experiences a varied response to quenching; more specifically that molecules with a higher Stokes shift will experience fewer quenching effects.

While the implication is that whole molecules of TMAda are no longer extant in the sample, this does not necessarily mean hydrocarbons are completely eradicated from the sample as it is possible that other molecules may have different emission signatures to TMAda. At this point, the following question offers itself for debate: is the emission measured from a calcined zeolite borne of trace carbon surviving the calcination, or is it merely an intrinsic photoluminescent signature of the framework? The presence of two residual Raman bands in Figure 3 at around 800 cm^{-1} show that it is possible there is a small amount of hydrocarbon material left in the sample, with the fluorescence spectra in Figure 7 reflecting the simpler molecular hydrocarbon configuration leftover in the zeolite cages. The lack of phosphorescence additionally implies that any hydrocarbon remaining is likely to be small relative to the size of the cages and perhaps even mobile within the pore structures, experiencing less confinement and subsequently not exhibiting any phosphorescence.

It is also possible that the PL emission originates from the framework itself, as supported by a series of studies conducted on other silica-based mesoporous structures. Glinka et al.[51] recorded a series of PL emission spectra from MCM-41 mesoporous sieves and noted the similarity in PL emission from silica nanoparticles, attributing the emission to non-bridging oxygen hole centres. The molecular sieves in this study do, however, utilise an OSDA in the synthesis process, so it is not entirely possible to exclude the contribution of emission from an organic molecule. Equally, there are other studies postulating that UV excitation can induce PL from defect sites in a one-photon process in non-templated silica based materials like silica particles[52], silicon quantum dots embedded in an array[53], bulk amorphous SiO_2[54,55,56,57], and fused silica[58].

Ultimately, it is the time-resolved aspect of this study that bolsters the conclusion that the emission arising in the calcined sample is likely to be coming from the framework. Previous comparisons with organic-heavy samples (i.e. uncalcined and intermediate samples) show that organic-based emission in zeolites is most characteristically defined by a fast-lived component that is no longer extant beyond the 10 ns window, a complex ensemble of emission profiles relating to the range of different species and decay pathways, and a phosphorescent component arising as a result of steric confinement. In contrast, the calcined sample appears to display a comparatively simple, single-source emission dynamic that experiences less change in the gated spectra, minimal difference in lifetime analysis across different spectral regions, and exhibits no phosphorescence. It is possible then that the PL signal in calcined CHA is arising due to defect sites in the aluminosilicate framework, representing an intrinsic zeolite emission. The overall intensity of the calcined sample is also significantly lower than the uncalcined material, implying that this intrinsic framework signal is being drowned by the more intense organic-based emission arising in the uncalcined material.

4. CONCLUSION

Detemplation of chabazite has been successfully studied using a sensitive TRPS method. Three signatures were established for the different samples:

1) A characteristic emission spectrum for the OSDA was established with a red-shift occurring upon confinement.
2) Phosphorescence signal can be used to signature the presence of occluded organic material.
3) An intrinsic zeolite emission related to framework defects is recorded in the calcined sample.

In future studies, it is envisioned that this technique will be able to inform researchers on other topical questions regarding adsorbed organics, a common example of which is the formation of carbonaceous deposits in catalytic reactions, which affect the conversion efficiency of acidic zeolites.[59] Proliferation of coke deposits are problematic as they have been correlated with progressive deactivation of the catalyst[60,61]. The flexibility of the setups mean it is also possible to accommodate *in-situ* operando studies of zeolite systems, which could form the basis of future experimentation.

AUTHOR INFORMATION

Corresponding Author

Prof Andrew M. Beale

E-mail: Andrew.beale@ucl.ac.uk

Author Contributions

The manuscript was written through contributions of all authors. All authors have given approval to the final version of the manuscript.

SUPPORTING INFORMATION AVAILABLE

Photographs of samples and additional Raman characterisation are available in supporting information.

ACKNOWLEDGMENTS

We should thank Johnson Matthey & EPSRC for funding a case award for Naomi Omori – voucher number 15220110. We also thank the EPSRC sponsored UK Catalysis Hub for funding the project of A. G. Greenaway (EP/K014714/1).We also acknowledge the help of Sara Mosca, Pavel Matousek, Daniela Comelli, Peixi Cong, and Ines Lezcano-Gonzalez

ABBREVIATIONS

CHA - Chabazite

CW – Continuous wave

PL - Photoluminescence

RTP – Room temperature phosphorescence

TRPS – Time resolved photoluminescence spectroscopy

TMAda – Trimethyladamantylammonium hydroxide

REFERENCES

(1) Vogt, E. T. C.; Weckhuysen, B. M. Fluid Catalytic Cracking: Recent Developments on the Grand Old Lady of Zeolite Catalysis. *Chem. Soc. Rev.* **2015**, *44*, 7342–7370.

(2) Tian, P.; Wei, Y.; Ye, M.; Liu, Z. Methanol to Olefins (MTO): From Fundamentals to Commercialization. *ACS Catal.* **2015**, *5*, 1922–1938.

(3) Amghizar, I.; Vandewalle, L. A.; Geem, K. M. Van; Marin, G. B. New Trends in Olefin Production. *Engineering* **2017**, *3*, 171–178.

(4) Haghseresht, F.; Lu, G. Q.; Whittaker, A. K. Carbon Structure and Porosity of Carbonaceous Adsorbents in Relation to Their Adsorption Properties. *Carbon N. Y.* **1999**, *37*, 1491–1497.

(5) C. H. Collett, J. M. Things Go Better with Coke: The Beneficial Role of Carbonaceous Deposits in Hetereogenous Catalysis. *Catal. Sci. Technol.* **2016**, *6*, 363–378.

(6) Rojo-Gama, D.; Nielsen, M.; Wragg, D. S.; Dyballa, M.; Holzinger, J.; Falsig, H.; Lundegaard, L. F.; Beato, P.; Brogaard, R. Y.; Lillerud, K. P.; et al. A Straightforward Descriptor for the Deactivation of Zeolite Catalyst H-ZSM-5. *ACS Catal.* **2017**, *7*, 8235–8246.

(7) Kosinov, N.; Uslamin, E. A.; Coumans, F. J. A. G.; Wijpkema, A. S. G.; Rohling, R. Y.; Hensen, E. J. M. Structure and Evolution of Confined Carbon Species during Methane Dehydroaromatization over Mo/ZSM-5. *ACS Catal.* **2018**, *8*, 8459–8467.

(8) Bordiga, S.; Lamberti, C.; Bonino, F.; Travert, A.; Thibault-Starzyk, F. Probing Zeolites by Vibrational Spectroscopies. *Chem. Soc. Rev.* **2015**, *44*, 7262–7341.

(9) Knops-Gerrits, P. P.; De Vos, D. E.; Feijen, E. J. P.; Jacobs, P. A. Raman Spectroscopy on Zeolites. *Microporous Mater.* **1997**, *8*, 3–17.

(10) Matousek, P.; Towrie, M.; Ma, C.; Kwok, W. M.; Phillips, D.; Toner, W. T.; Parker, A. W. Fluorescence Suppression in Resonance Raman Spectroscopy Using a High-Performance Picosecond Kerr Gate. *J. Raman Spectrosc.* **2001**, *32*, 983–988.

(11) Liu, D. R.; Gao, Z. H.; Zi, W. W.; Zhang, J.; Du, H. Bin; Chen, F. J. Facile Synthesis of Large-Pore Zeolite ITQ-26 by Using an Easily-Available Imidazolium as Structure-Directing Agent. *Microporous Mesoporous Mater.* **2019**, *276*, 232–238.

(12) Hashimoto, S. Zeolite Photochemistry: Impact of Zeolites on Photochemistry and Feedback from Photochemistry to Zeolite Science. *J. Photochem. Photobiol. C Photochem. Rev.* **2003**, *4*, 19–49.

(13) Yamashita, H.; Matsuoka, M.; Tsuji, K.; Shioya, Y.; Anpo, M.; Che, M. In-Situ XAFS, Photoluminescence, and IR Investigations of Copper Ions Included within Various Kinds of Zeolites. Structure of Cu(I) Ions and Their Interaction with CO Molecules. *J. Phys. Chem.* **1996**, *100*, 397–402.

(14) Matsuoka, M.; Anpo, M. Photoluminescence Properties and Photocatalytic Reactivities of Cu+/Zeolite and Ag+/Zeolite Catalysts Prepared by the Ion-Exchange Method. *Curr. Opin. Solid State Mater. Sci.* **2003**, *7*, 451–459.

(15) Remillard, J. T.; Poindexter, B. D.; Weber, W. H. Fluorescence Characteristics of Cu-ZSM-5 Zeolites in Reactive Gas Mixtures: Mechanisms for a Fiber-Optic-Based Gas Sensor. *Appl. Opt.* **1997**, *36*, 3699–3707.

(16) Coutiño-Gonzalez, E.; Baekelant, W.; Steele, J. A.; Kim, C. W.; Roeffaers, M. B. J.; Hofkens, J. Silver Clusters in Zeolites: From Self-Assembly to Ground-Breaking Luminescent Properties. *Acc. Chem. Res.* **2017**, *50*, 2353–2361.

(17) Li, H.; Li, P. Luminescent Materials of Lanthanoid Complexes Hosted in Zeolites. *Chem.*

Commun. **2018**, *54*, 13884–13893.

(18) Lin, H. Y.; Chin, C. Y.; Huang, H. L.; Huang, W. Y.; Sie, M. J.; Huang, L. H.; Lee, Y. H.; Lin, C. H.; Lii, K. H.; Bu, X.; et al. Crystalline Inorganic Frameworks with 56-Ring, 64-Ring, and 72-Ring Channels. *Science (80-.).* **2013**, *339*, 811–813.

(19) Li, H.; Ding, Y.; Wang, Y. Photoluminescence Properties of Eu3+-Exchanged Zeolite L Crystals Annealed at 700 °c. *CrystEngComm* **2012**, *14*, 4767–4771.

(20) Ruivo, A.; Coutino-Gonzalez, E.; Santos, M. M.; Baekelant, W.; Fron, E.; Roeffaers, M. B. J.; Pina, F.; Hofkens, J.; Laia, C. A. T. Highly Photoluminescent Sulfide Clusters Confined in Zeolites. *J. Phys. Chem. C* **2018**, *122*, 14761–14770.

(21) Planells, A.; You, J.; Triplett, G.; Hunt, H. K. Investigation of the Photoluminescence of Microporous Silicalite-1 (MFI) Films. *Microporous Mesoporous Mater.* **2016**, *220*, 73–80.

(22) Wang, M.; Gu, S.; Jiang, W.; Lin, H.; Fan, Y. Origin of Ultraviolet Photoluminescence in Zeolite-Derived Glass. *J. Non. Cryst. Solids* **2017**, *471*, 462–466.

(23) Wang, L.; Jiang, W.; Chen, L.; Shen, Z. Formation of a Unique Glass by Spark Plasma Sintering of a Zeolite. *J. Mater. Res.* **2009**, *24*, 3241–3245.

(24) Dozzi, M. V.; D'Andrea, C.; Ohtani, B.; Valentini, G.; Selli, E. Fluorine-Doped TiO2 Materials: Photocatalytic Activity vs Time-Resolved Photoluminescence. *J. Phys. Chem. C* **2013**, *117*, 25586–25595.

(25) Karwacki, L.; Weckhuysen, B. M. New Insight in the Template Decomposition Process of Large Zeolite ZSM-5 Crystals: An in Situ UV-Vis/Fluorescence Micro-Spectroscopy Study. *Phys. Chem. Chem. Phys.* **2011**, *13*, 3681–3685.

(26) Warringham, R.; Gerchow, L.; Zubiaga, A.; Cooke, D.; Crivelli, P.; Mitchell, S.; Pérez-Ramírez, J. Insights into the Mechanism of Zeolite Detemplation by Positron Annihilation

Lifetime Spectroscopy. *J. Phys. Chem. C* **2016**, *120*, 25451–25461.

(27) Dent, L.; Smith, J. Crystal Structure of Chabazite, a Molecular Sieve. *Nature* **1958**, *181*, 1794–1796.

(28) Baerlocher, C.; McCusker, L. Database of Zeolite Structures http://www.iza-structure.org/databases/.

(29) Beale, A. M.; Lezcano-Gonzalez, I.; Slawinksi, W. A.; Wragg, D. S. Correlation between Cu Ion Migration Behaviour and DeNOxactivity in Cu-SSZ-13 for the Standard NH3-SCR Reaction. *Chem. Commun.* **2016**, *52*, 6170–6173.

(30) Greenaway, A. G.; Gonzalez, I. L.; Aran, M. A.; Gibson, E. K.; Odarchenko, Y.; Beale, A. M. Operando Spectroscopic Studies of Cu – SSZ-13 for - NH 3 – SCR DeNOx Investigates the Role of - NH 3 in Observed Cu (II) Reduction at High NO Conversions. *Top. Catal.* **2018**, *61*, 175–182.

(31) Systems, D. Biovia Materials Studio. 5005 Wateridge Vista Drive, San Diego, CA 92121 USA 2017.

(32) Sun, H. COMPASS: An Ab Initio Force-Field Optimized for Condensed-Phase ApplicationsOverview with Details on Alkane and Benzene Compounds. *J. Phys. Chem. B* **1998**, *102*, 7338–7364.

(33) Stevens, A. P.; Gorman, A. M.; Freeman, C. M.; Cox, P. A. Prediction of Template Location via a Combined Monte Carlo–Simulated Annealing Approach. *J. Chem. Soc. Faraday Trans.* **1996**, *92*, 2065–2073.

(34) Dozzi, M. V.; Candeo, A.; Marra, G.; D'Andrea, C.; Valentini, G.; Selli, E. Effects of Photodeposited Gold vs Platinum Nanoparticles on N,F-Doped TiO2Photoactivity: A Time-Resolved Photoluminescence Investigation. *J. Phys. Chem. C* **2018**, *122*, 14326–14335.

(35) Ware, W. R.; Cunningham, P. T. Lifetime and Quenching of Anthracene Fluorescence in the Vapor Phase. *J. Chem. Phys.* **1965**, *43*, 3826–3831.

(36) Hashimoto, S.; Yamaji, M. Observation of Intramolecular Singlet and Triplet Excimers of Tethered Naphthalene Moieties under the Geometric Constraints Imposed by the Host Framework of Zeolites. *Phys. Chem. Chem. Phys.* **2008**, *10*, 3124–3130.

(37) Hashimoto, S.; Fukazawa, N.; Fukumura, H.; Masuhara, H. Observation and Characterization of Excimer Emission from Anthracene Included in NaX Zeolite. *Chem. Phys. Lett.* **1994**, *219*, 445–451.

(38) Bilger, S.; Soulard, M.; Kessler, H.; Guth, J. L. Identification of the Volatile Products Resulting from the Thermal Decomposition of Tetra-, Tri-, Di-, and Mono-n-Propylammonium Cations Occluded in MFI-Type Zeolites. *Zeolites* **1991**, *11*, 784–791.

(39) Jenkins, T. E.; Lewis, J. A Raman Study of Adamantane (C10H16), Diamantane (C14H20) and Triamantane (C18H24) between 10 K and Room Temperatures. *Spectrochim. Acta Part A Mol. Spectrosc.* **1980**, *36*, 259–264.

(40) Krishnamurti, D. The Raman Spectrum of Quartz and Its Interpretation. *Proc. Indian Acad. Sci. - Sect. A* **1958**, *47*, 276–291.

(41) Krishnan, R. S. Raman Spectrum of Quartz. *Nature* **1945**, *155*, 452.

(42) Xiao, C.; Du, Y.; Dong, L.; Zhou, X.; Xie, Y.; Tan, Z. PdO x /Silicalite-1 Catalyst Prepared by Room Temperature Ozone Treatment: Preparation Chemistry and Catalytic Performance for Methane Combustion. *Catal. Letters* **2017**, *147*, 1775–1782.

(43) Miecznikowski, A.; Hanuza, J. Infrared and Raman Studies of ZSM-5 and Silicalite-1 at Room, Liquid Nitrogen and Helium Temperatures. *Zeolites* **1987**, *7*, 249–254.

(44) Kalita, A.; Deka, K.; Kalita, M. P. C. On the Influence of Raman Scattering of Water in the

Photoluminescence Measurement of Water Dispersed ZnO Nanocrystals. *Methods Appl. Fluoresc.* **2017**, *5*.

(45) Ramamurthy, V.; Caspar, J. V; Eaton, D. F.; Kuo, E. W.; Corbin, D. R. Heavy-Atom-Induced Phosphorescence of Aromatics and Olefins Included within Zeolites. *J. Am. Chem. Soc.* **1992**, *114*, 3882–3892.

(46) Ramamurthy, V.; Turro, N. J. Photochemistry of Organic Molecules within Zeolites: Role of Cations. *J. Incl. Phenom. Mol. Recognit. Chem.* **1995**, *21*, 239–282.

(47) Casal, H. L.; Scaiano, J. C. Intrazeolite Photochemistry. I. Phosphorescence Enhancement of Aromatic Ketones Included in Silicalite. *Can. J. Chem.* **1984**, *62*, 628–629.

(48) Kobayashi, S.; Sidike, A.; Yamashita, N. Luminescence Spectra of Chabazite-Ca, a Zeolite Mineral. *Phys. Chem. Miner.* **2012**, *39*, 465–470.

(49) Grandjean, D.; Coutiño-Gonzalez, E.; Cuong, N. T.; Fron, E.; Baekelant, W.; Aghakhani, S.; Schlexer, P.; D'Acapito, F.; Banerjee, D.; Roeffaers, M. B. J.; et al. Origin of the Bright Photoluminescence of Few-Atom Silver Clusters Confined in LTA Zeolites. *Science.* **2018**, *361*, 686–690.

(50) Qian, Q.; Mores, D.; Kornatowski, J.; Weckhuysen, B. M. Template Removal Processes within Individual Micron-Sized SAPO-34 Crystals: Effect of Gas Atmosphere and Crystal Size. *Microporous Mesoporous Mater.* **2011**, *146*, 28–35.

(51) Glinka, Y. D.; Lin, S.-H.; Hwang, L.-P.; Chen, Y.-T. Photoluminescence Spectroscopy of Silica-Based Mesoporous Materials. *J. Phys. Chem. B* **2002**, *104*, 8652–8663.

(52) Xu, G. Q.; Zheng, Z. X.; Tang, W. M.; Wu, Y. C. Multi-Peak Behavior of Photoluminescence of Silica Particles Heat-Treated in Hydrogen at Elevated Temperature. *J. Lumin.* **2007**, *126*, 43–47.

(53) Lu, S.; Wu, B.; Sun, Y.; Cheng, Y.; Liao, F.; Shao, M. Photoluminescence of Pure Silicon Quantum Dots Embedded in an Amorphous Silica Wire Array. *J. Mater. Chem. C* **2017**, *5*, 6713–6717.

(54) Hosono, H.; Kawazoe, H.; Matsunami, N. Experimental Evidence for Frenkel Defect Formation in Amorphous SiO2 by Electronic Excitation. *Phys. Rev. Lett.* **1998**, *80*, 317–320.

(55) Itoh, C.; Tanimura, K.; Itoh, N.; Itoh, M. Threshold Energy for Photogeneration of Self-Trapped Excitons in SiO2. *Phys. Rev. B* **1989**, *39*, 11183–11186.

(56) Skuja, L.; Güttler, B. Detection of Interstitial Oxygen Molecules in SiO2 Glass by a Direct Photoexcitation of the Infrared Luminescence of Singlet O2. *Phys. Rev. Lett.* **1996**, *77*, 2093–2096.

(57) Pacchioni, G.; Ieraño, G. Ab Initio Theory of Optical Transitions of Point Defects in SiO2. *Phys. Rev. B* **1998**, *57*, 818–832.

(58) Griscom, D. L.; Mizuguchi, M. Determination of the Visible Range Optical Absorption Spectrum of Peroxy Radicals in Gamma-Irradiated Fused Silica. *J. Non. Cryst. Solids* **1998**, *239*, 66–77.

(59) Guisnet, M.; Magnoux, P. Fundamental Description of Deactivation and Regeneration of Acid Zeolites. *Stud. Surf. Sci. Catal.* **1994**, *88*, 53–68.

(60) Goetze, J.; Meirer, F.; Yarulina, I.; Gascon, J.; Kapteijn, F.; Ruiz-Martínez, J.; Weckhuysen, B. M. Insights into the Activity and Deactivation of the Methanol-to-Olefins Process over Different Small-Pore Zeolites As Studied with Operando UV-Vis Spectroscopy. *ACS Catal.* **2017**, *7*, 4033–4046.

(61) Qi, G.; Xie, Z.; Yang, W.; Zhong, S.; Liu, H.; Zhang, C.; Chen, Q. Behaviors of Coke

Deposition on SAPO-34 Catalyst during Methanol Conversion to Light Olefins. *Fuel Process. Technol.* **2007**, *88*, 437–441.

TOC GRAPHIC

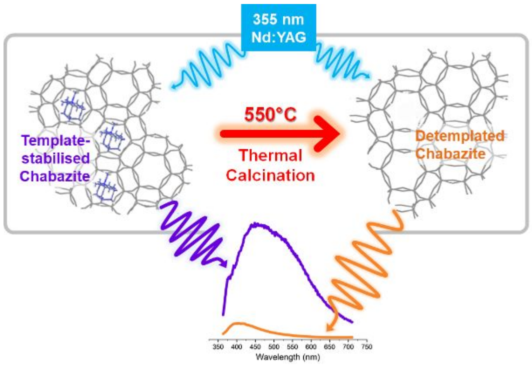
355 nm
Nd:YAG
550°C
Thermal
Calcination
Template-
stabilised
Chabazite
Detemplated
Chabazite
350
400
450
500
550
600
650
700
750
Wavelength (nm)